Geophysical Journal International

Geophys. J. Int. (2018) **213,** 836–850
Advance Access publication 2018 January 19
GJI Marine geosciences and applied geophysics

doi: 10.1093/gji/ggy017

Multimode seismoelectric phenomena generated using explosive and vibroseis sources

Karl E. Butler,[1] Bernd Kulessa[2] and André J.-M. Pugin[3]

[1]*Department of Earth Sciences, University of New Brunswick, P.O. Box* 4400, *Fredericton, New Brunswick* E3B 5A3, *Canada. E-mail: kbutler@unb.ca*
[2]*College of Science, Swansea University, Singleton Park, Swansea,* SA2 8PP *Wales, UK*
[3]*Geological Survey of Canada–NRC,* 601 *Booth Street, Ottawa, Ontario* K1A 0E8, *Canada*

Accepted 2018 January 18. Received 2017 December 16; in original form 2017 May 19

SUMMARY

A field trial of seismoelectric surveying was carried out at a site underlain by 20 m of water-saturated clayey Champlain Sea sediments, renowned for their amenability to high resolution imaging by seismic reflection surveys. Seismically induced electrokinetic effects were recorded using an array of 26 grounded dipole electric field antennas, and two different seismic sources including an eight-gauge shotgun, and a moderate power (10 000 lb Minivib) vibrator. Despite the high electrical conductivity of the sediments, shot records show evidence of possible interfacial seismoelectric conversions caused by the arrival of *P*-waves at the base of the clay/top of bedrock and at the top of a layer of elevated porosity and conductivity within the clay at 7 m depth. However, the data are more remarkable for the fact that *P*-wave, *S*-wave, and *PS*/*SP* converted wave reflections evident in the seismic records all give rise to electrical arrivals exhibiting very similar moveout patterns in the seismoelectric records. Superficially, these electrical responses could be misinterpreted as simple coseismic seismoelectric effects associated with the arrival of reflected seismic waves at each dipole antenna on surface. However, their broader bandwidth, superior coherency and earlier arrival times compared to their corresponding seismic arrivals indicate that the electrical effects are generated by the arrival of seismic reflections below each dipole at the shallow intraclay interface 7 m below surface. Such quasi-coseismic arrivals have recently been predicted by full-waveform seismoelectric modelling and characterized as evanescent electromagnetic (EM) waves. In retrospect, they were also observed in earlier seismoelectric field trials, but not measured as clearly nor recognized as a distinct seismoelectric mode intermediate between interfacial and coseismic effects. We propose that the observed quasi-coseismic effect can be understood physically as a fringing field emanating from the travelling charge separation associated with a *P*-wave (direct or mode-converted) crossing a subsurface interface at an oblique angle. Such effects may be nearly indistinguishable from coseismic effects if the interface depth is small compared to the seismic wavelength, but recognition of the phenomenon contributes to an improved understanding of the seismoelectric wavefield, and will lead to improved interpretations. From a practical standpoint, the results of this field trial suggest that using electric field receivers to supplement geophones on surface could yield significantly higher resolution seismic reflection images in those areas where suitable near-surface layers exist for the generation of quasi-coseismic effects. The results also reinforce the importance of using multichannel recording to allow interfacial seismoelectric conversions originating at depth to be distinguished from stronger coseismic and quasi-coseismic arrivals originating in the near-surface by measurement of their arrival time versus offset (moveout) and amplitude versus offset behaviours.

Key words: Electrical properties;; Hydrogeophysics; Electromagnetic theory; Body waves; Interface waves; Wave propagation .

1 INTRODUCTION

Electrokinetic effects induced by seismic waves are of interest in groundwater, oil and gas, geotechnical and glaciological investigations for their dependence on fluid flow permeability and their potential to combine the resolution of seismic methods with the sensitivity of electrical methods to pore fluid properties. Although first reported in the 1930s, there has been an acceleration in

theoretical and experimental developments since the early 1990s when Thompson & Gist (1993) presented field data and arguments suggesting that the seismoelectric method can be used to image porous, permeable hydrocarbon reservoirs. Most of the follow-up studies have utilized low energy sources and targeted the detection of high permeability formations. Results of these near-surface field experiments have been mixed—offering encouraging evidence of the ability to image shallow interfaces at depths less than 20 m but also the recognition that it is a challenge to identify interfacial signals in the presence of ambient noise and coseismic effects that are commonly much stronger. Other potential areas of application that have received attention through experimental studies include well logging (e.g. Hunt & Worthington 2000; Mikhailov *et al.* 2000; Singer *et al.* 2006; Dupuis & Butler 2006; West 2012; Zhu & Toksöz 2012), vadose zone hydrogeology (e.g. Dupuis *et al.* 2007; Strahser *et al.* 2011; Bordes *et al.* 2015), glaciology (Kulessa *et al.* 2006; Siegert *et al.* 2017) and permafrost detection (Liu *et al.* 2008). Potential applications in cross-hole imaging (Zhu & Toksöz 2003; Haines & Pride 2006; Araji *et al.* 2012; Sava *et al.* 2014), detection of thin geological layers (Haines & Pride 2006; Grobbe & Slob 2016), beamform imaging (El Khoury *et al.* 2015), characterization of heavy oil reservoirs (Revil & Jardani 2010) and in well logging (Guan *et al.* 2013; Zyserman *et al.* 2015) have been explored through modelling. Developments in understanding, geophysical modelling and measurement of seismoelectromagnetic effects of electrokinetic origin are reviewed in recent publications by Revil *et al*. (2015), and Jouniaux & Zyserman (2016).

Theoretical considerations and experimental observations confirm that electrokinetic effects can be induced by a variety of seismic wave types including compressional, shear, and surface waves as well as guided waves in boreholes. Much of the focus in research has been on the potential for imaging interfaces or other targets at depth using seismic sources and electromagnetic receivers on the ground surface, in a manner analogous to seismic reflection surveying. *P*-waves or *S*-waves could, in principle, be used in that type of survey mode, as affirmed by theoretical modelling at seismic frequencies (Haartsen & Pride 1997; Garambois & Dietrich 2002). The interfacial E-fields produced by *S*-waves emanating from a vertical seismic source are, however, expected to be about an order of magnitude smaller than those produced by the *P*-waves emanating from the same source (Warden *et al.* 2013). In addition, we note that magnetic measurements would suffer interference from seismic shaking of sensors in the earth's magnetic field. For those reasons, field trials have focussed on the use of *P*-waves and electric field receivers, although magnetic fields associated with *S*-waves have been observed during an experiment in an ultralow-noise laboratory (Bordes *et al.* 2008).

1.1 Electrokinetic effects induced by *P*-waves

Seismically induced electrokinetic coupling in porous media arises from motion of charge in the electrical double layer at the solid–liquid interface (Pride 1994). Compressional waves cause pore fluid to move relative to the solid matrix, thereby moving the excess electrical charge in the outer, mobile portion of the electrical double layer. These streaming currents result in charge separations and hence electrical fields arising between zones of compression and rarefaction. In a homogeneous medium, this phenomenon gives rise to a coseismic electric field that is confined within the compressional wave (e.g. Frenkel 1944; Neev & Yeatts 1989; Pride & Haartsen 1996; Garambois & Dietrich 2001; Dupuis & Butler 2006; Gershenzon *et al.* 2014). When a compressional wave encounters heterogeneity such as an interface that changes the streaming currents and distorts the resulting charge distribution, it generates an unbounded electric field, which we call an interfacial seismoelectric effect (e.g. Butler *et al*. 1996; Haartsen & Pride 1997; Garambois & Dietrich 2002; Dupuis *et al*. 2009; Warden *et al*. 2013). This field is expected to propagate (diffuse) through the earth as an electromagnetic signal and therefore appear nearly simultaneously at widely separated receivers with an arrival time only marginally greater than the one-way seismic traveltime from shotpoint to interface. Quasi-coseismic signals, such as those known to emanate from critically refracted *P*-waves travelling beneath electric field receivers (e.g. Butler 1996; Mikhailov *et al.* 1997) represent a third, albeit less well documented, type of seismoelectric effect. Ren *et al.* (2015) recently used theoretical and full waveform seismoelectric modelling to predict that similar quasi-coseismic effects, representing evanescent EM waves, should be generated by *P* and *S* wave fronts spreading along interfaces at oblique angles; they predicted that the quasi-coseismic EM fields attenuate exponentially with distance normal to the interface such that they would only be detectable by antennas at relatively short range, and might therefore be indistinguishable from coseismic arrivals.

Conceptual and full waveform numerical models (e.g. Butler *et al.* 1996; Haartsen & Pride 1997; Garambois & Dietrich 2002) indicate that the interfacial effect should be a multipole electrical source that develops over a Fresnel zone having a diameter that increases with depth and seismic wavelength. Higher order terms will diminish more rapidly with distance leaving the dipole term to dominate. Thus, an interfacial seismoelectric signal emanating from a planar horizontal interface is expected to exhibit symmetry and amplitude characteristics similar to that of a vertical electrical dipole centred on that interface directly below the shotpoint. The vertical dipole-like model for interfacial seismoelectric sources is supported by measurements of signal amplitude versus receiver offset (AVO) at the ground surface (e.g. Butler *et al*. 1996; Dupuis *et al.* 2007; Strahser *et al.* 2007) and amplitude versus receiver depth in a borehole (Dupuis *et al.* 2009). However, recent lab experiments by Schakel *et al.* (2012) have reinforced the observation by Dupuis *et al.* (2007) that the rate of decay of signal amplitude with offset is slightly less than predicted by the simple vertical dipole model.

The types of interfaces (i.e. physical property contrasts) most likely to yield seismoelectric conversions are not yet well established as a change in seismically induced streaming current density can be generated by contrasts in a wide range of seismic and electrical properties (e.g. acoustic impedance, porosity, permeability, electrical conductivity, zeta potential) or by changes in the pore fluid type. Numerical modelling (e.g. Haartsen & Pride 1997; Garambois & Dietrich 2002; Pride & Garambois 2002; Haines & Pride 2006; Warden *et al.* 2013) has offered insight but is also complicated by the fact that some physical properties are functions of multiple others. Thompson *et al.* (2007) state that the three main conditions favouring production of a strong seismoelectric conversion are a contrast in acoustic impedance in the presence of a permeable pore space (favouring the production of Biot slow waves), and high-resistivity pore fluids (yielding relatively strong electric fields from a streaming current source).

1.2 Field observations of interfacial seismoelectric effects

It is also instructive to consider the types of targets that have yielded interfacial effects during field experiments. We restrict

the discussion here to those field experiments that have demonstrated convincing evidence of electrokinetic seismoelectric conversion in terms of expected signal moveout, and AVO characteristics. Martner & Sparks (1959) were the first investigators to report interfacial seismoelectric effects likely to be electrokinetic in origin. They attributed them to the arrival of *P*-waves at the base of the seismic weathered layer where there was a significant increase in *P*-wave velocity. The geological nature of the interface (located at depths of 3–17 m in their examples from central and southern Oklahoma) was not investigated except to confirm that it was not merely the water table. The reported subweathering *P*-wave velocities of 6.0–7.5 ft ms^{-1} (1800–2300 m s^{-1}) are suggestive of compacted water-saturated sediments or weakly consolidated rock, which would be expected to have a higher acoustic impedance and lower porosity than the weathered layer above. Similarly, Butler *et al.* (1996), Russell *et al.* (1997) and Mikhailov *et al.* (1997) demonstrated that interfacial seismoelectric effects were generated at large contrasts in acoustic impedance between loose surficial fill/soils and underlying glacial till layers (again independent of water table depth). Garambois & Dietrich (2001) and Strahser *et al.* (2007) reported on interfacial responses in alluvial sediments that they attributed to the water table and to a thin silt layer within water-saturated sands, respectively. Haines *et al.* (2007) conducted a highly controlled field experiment under partially saturated conditions to measure interfacial responses from two sand-filled trenches having porosities, permeabilities, electrical conductivities and *P*-wave velocities that contrasted with the surrounding clayey soils. Dupuis *et al.* (2007) measured interfacial responses from depths of approximately 7 and 15 m in the vadose zone of an unconfined sand aquifer and demonstrated that they could be traced laterally along a profile 300 m long. The shallower interface was a water retentive layer, while the lower interface was the water table—both of which were commonly associated with partial cementation of the sand (Dupuis *et al.* 2007, 2009). Thus, cementation-related acoustic impedance contrasts may have augmented water-saturation-related contrasts in giving rise to the interfacial effects. Moreover, as confirmed by recent modelling studies (Warden *et al.* 2013), the relatively coarse sediment texture (favouring development of a strong gradient in water saturation at the water table), together with the presence of dry surficial sediments (limiting the amplitudes of coseismic interference from direct *P*-waves and surface waves), would have been favourable for the generation and detection of interfacial effects at the site.

All of the above field experiments were focussed on near surface targets within the upper 20 m of the subsurface. A much larger scale field trial, employing high energy explosive sources and receivers distributed over 600 m on surface was conducted by Exxon researchers (Thompson & Gist 1993). No shot records were presented to illustrate signal moveout or AVO characteristics, but the authors did generate a stacked seismoelectric section that appears to image several interfaces within a sequence of water-saturated sands and shales exhibiting contrasts in permeability and acoustic impedance at depths of up to 300 m. More recent large scale field experiments, carried out by Dean & Dupuis (2011) and Dean *et al*. (2012) over aquifer targets in arid environments, demonstrated that large vibroseis sources (60 000–80 000 lb peak force) could be used successfully to extend the offset range and time window for seismoelectric recording. However, while the shallow vadose zone interfacial effects previously recorded by Dupuis *et al*. (2007) were reproduced at one site, attempts to identify interfacial effects from greater depths were more speculative due to overprinting by coseismic arrivals.

1.3 Motivation

The geological environment for this study near Ottawa, Canada, was very different from those investigated in previous publications. It consisted of approximately 20 m of soft clays and silts overlying a thin layer of diamicton/glacial till capping bedrock. Although a large contrast in acoustic impedance was known to be present at the bedrock surface, the high conductivities and low permeabilities expected of the overlying fine-grained sediments were not considered optimal for the production of strong seismoelectric conversions as outlined above. Nevertheless, we were encouraged to proceed with field trials at the site for three reasons. First, given the relatively untested nature of models for seismoelectric conversion, it is important to investigate sites having physical properties very different from those considered previously. Second, we were able to take advantage of the availability of a moderately powerful (10 000 lb peak force) vibroseis source operated by the Geological Survey of Canada. This promised to provide significantly more seismic energy than the typical impact sources used in most previous near surface seismoelectric studies, although there was uncertainty over whether it might also generate problematic electrical noise. Third, the site's subsurface conditions were well-characterized; geotechnical and *S*-wave velocity borehole logs were available, and multicomponent seismic reflection and electrical resistivity data could be readily acquired to assess lateral homogeneity. The soft Champlain Sea sediments in the area were renowned for yielding remarkably high resolution seismic reflection data including *P*, *S* and *PS* converted wave reflections. The logs together with seismic reflection and electrical resistivity data would constrain interpretation of the seismoelectric data. Interfacial targets of interest included the overburden/bedrock contact as well as shallower interfaces associated with porosity, grain size, and *S*-wave velocity changes within the overburden.

2 GEOLOGICAL SETTING

Seismoelectric experiments were conducted in late May 2011 on the grounds of the former Canadian Forces Station Gloucester and current Royal Canadian Legion at 8021 Mitch Owens Road, Gloucester, Ontario, 21 km southeast of Ottawa. Seismoelectric and electrical resistivity tomography (ERT) data were acquired along an N–S oriented survey line (Fig. 1) located in grass along the western edge of a paved road and parking lot, approximately 180 m west of the test fill that lies at the centre of NRC Geotechnical Research Site #1 (McRostie & Crawford 2001). Topography along the line was essentially flat, with minor surface undulations of less than half a metre caused by previous site activities. The grass was, in some places, underlain by weathered asphalt penetrated by our electrodes and geophones spikes.

Regional geological mapping (Harrison & MacDonald 1980) indicates that bedrock geology in the area consists of Ordovician clastics and carbonates. Overburden is dominated by a sequence of post-glacial clays and silts, known informally as Leda Clay—a glaciomarine–marine–estuarine sequence which records a transition from deep water, high salinity conditions to estuarine conditions as the Champlain Sea receded approximately 10 000 yr ago following retreat of the Laurentide ice sheet (Gadd 1986; Hunter *et al.* 2010).

Detailed descriptions of the surficial sediments underlying the study site are given by Bozozuk & Leonards (1972) and Lo *et al.* (1976) who presented geotechnical logs of the overburden derived from piston sampling to refusal at 20.4 m depth. They reported the presence of a 'surface crust', terminating abruptly at 1.8 m depth consisting of organic topsoil covering fine sand and silt and a basal

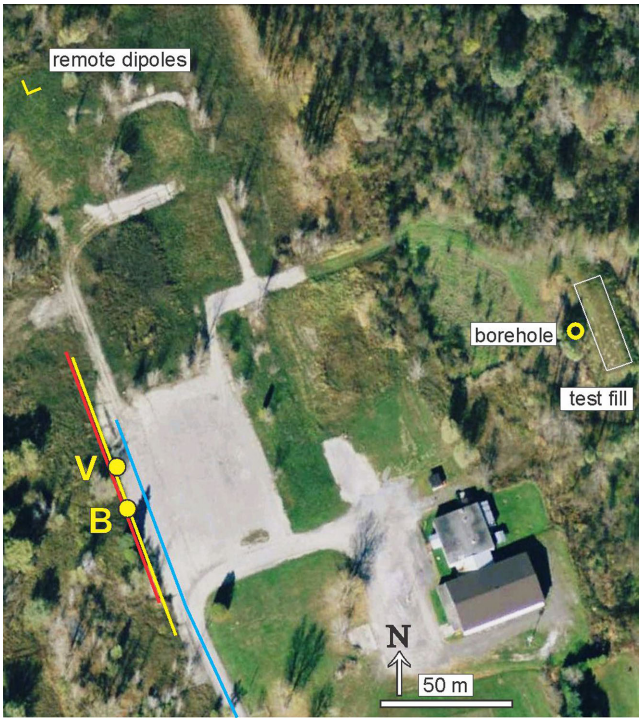

Figure 1. Aerial photo of the study site near Ottawa, showing positions of the seismoelectric recording array (yellow line), the ERT section (red line), the microvibe seismic section (blue line extending 140 m off the map), the remote dipoles and borehole BH-NRC-MO at the NRC Geotechnical Test Site. Points B and V are the midpoints of supergathers acquired using buffalo gun and vibroseis sources, respectively.

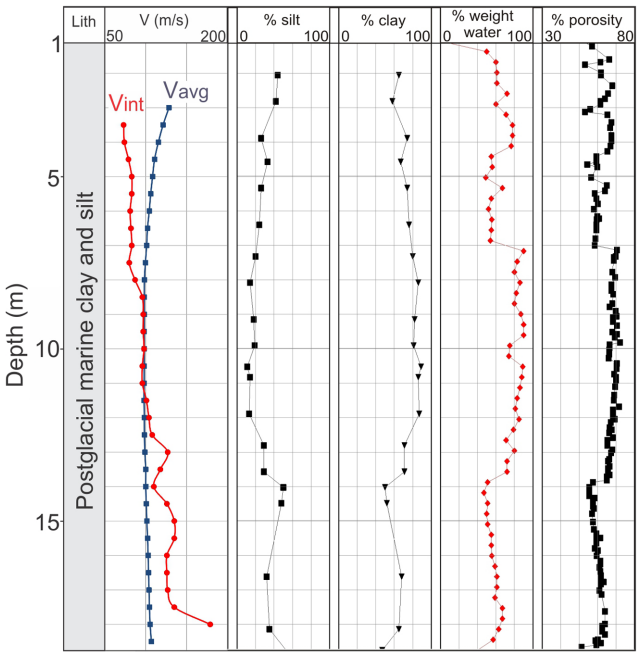

Figure 2. Shear wave velocity logs from borehole BH-NRC-MO and geotechnical data from samples collected in several boreholes around the NRC test fill. The figure is adapted from Lo *et al.* (1976) and Hunter *et al.* (2010). Porosities were calculated from weight per cent water contents assuming a specific gravity of 2.65 for the solid and a saturation of 100 per cent.

layer of desiccated grey-brown silty clay. Hunter *et al.* (2010) note that this crust is commonly present in the Ottawa area. It is interpreted to represent over-consolidated Champlain Sea deposits and is characterized by relatively high shear wave velocities. Very low shear strengths immediately below the crust generally increase with depth through a series of silty clay and clay layers to a depth of 18.3 m which we interpret to be the base of the Leda Clay. This was underlain by a thin layer (0.5 m) of varved clays and silts (likely lacustrine deposits recognized by Gadd 1986), and a heterogeneous deposit of grey clay, silt, sand and small stones classified as diamicton by Hunter *et al.* (2010) which we interpret to be the glacial till typically observed at the base of the Quaternary sequence in the Ottawa area (Gadd 1986; Hunter *et al.* 2010). Piston sampling returned 1.6 m of diamicton before refusal, indicating a depth to bedrock of 20.4 m or greater.

Fig. 2 presents porosity and clay/silt content logs from a compilation of boreholes surrounding the geotechnical test fill, (Bozozuk & Leonards 1972; Lo *et al.* 1976), as well as a shear wave velocity log from borehole BH-NRC-MO identified in Fig. 1. The latter was derived from measurements of shear wave arrivals generated using a sledgehammer source on surface, resolvable below 3 m depth using a three-component borehole geophone (Hunter *et al.* 2010). Average velocities (from surface) Vs_{avg} were calculated from the arrival time of shear waves at each depth, while interval velocities Vs_{int} represent *in situ* shear wave velocities based on arrival time differences. Estimated uncertainties in Vs_{int} are less than 5 per cent and in most cases less than 2 per cent (Hunter, private communication, 2013). The plot of Vs_{avg} supports the presence of a high velocity layer above 3 m depth, consistent with the presence of a surface crust. With some exceptions, interval velocities tend to increase with depth below 3 m but they are low by any standard, varying between 73 and 135 m s^{-1}, and jumping to a maximum of 180 m s^{-1} at 18 m (base of the Leda Clay). Closer inspection reveals three main sediment packages, separated by boundaries at ∼7 and 13.5 m, within which the interval velocities are relatively uniform. These packages align quite closely with those defined by clay/silt content and porosity. The middle layer between ∼7 and 13.5 m depth exhibits anomalously high clay contents and porosities in excess of 80 per cent and ∼ 70 per cent respectively. The overlying and underlying layers have lower clay contents and porosities although they are still high (60–80 per cent clay and 55–65 per cent porosity).

3 SEISMIC AND ELECTRICAL SITE CHARACTERIZATION

Multicomponent seismic reflection and electrical resistivity surveys were carried out in order to confirm the predominantly 1-D (layered) nature of the sediments, and identify the dominant seismic impedance contrasts and the electrical resistivity structure expected to influence seismoelectric fields.

3.1 Seismic reflectivity

Champlain Sea/Leda Clay sediments are characterized by very low shear wave velocities often $\ll$200 m s^{-1}, compressional-wave velocities comparable to the speed of sound in water (∼1500 m s^{-1}), and very low absorption (Pugin *et al.* 2009; Hunter *et al.* 2010). As a consequence, various compressional and shear wave phases are readily identified in high resolution multicomponent seismic reflection surveys (e.g. Pugin *et al.* 2013; Pugin & Yilmaz 2017).

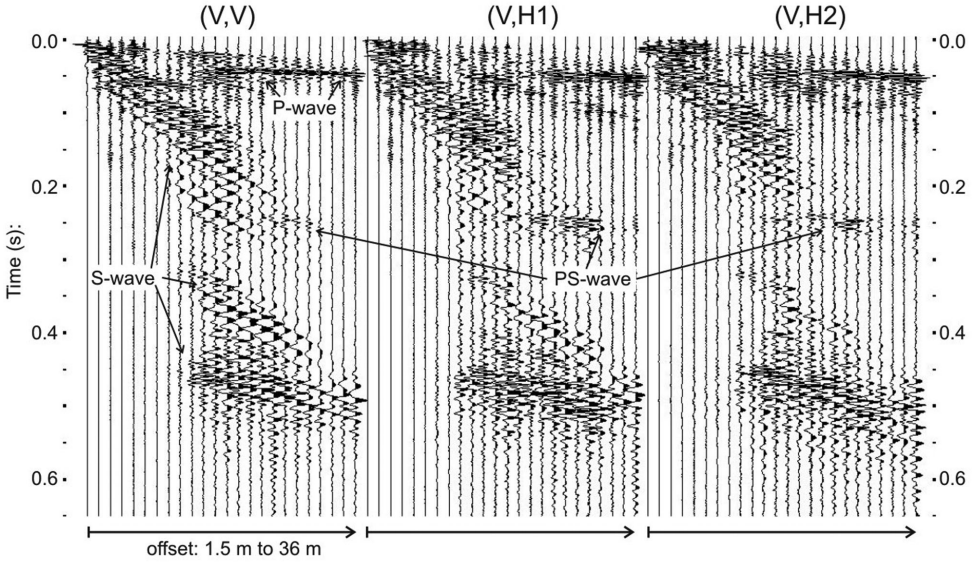

Figure 3. Sample high resolution seismic shot record recorded at the site using the Microvibe source shaking vertically and 24 three-component geophones mounted on a landstreamer at 1.5 m intervals. H1 and H2 refer to horizontal components in the inline and crossline directions, respectively. The record shows *P*-wave and *PS*-wave reflections from bedrock as well as several *S*-wave reflections exhibiting much greater moveout and later arrivals times due to the low *S*-wave velocities.

Fig. 3 shows a sample shot record acquired at this site in July 2012 using the Geological Survey of Canada's novel portable Microvibe source (Pugin *et al.* 2013) and 24 30-Hz three-component geophones spaced 1.5 m apart on a towed landstreamer. The Microvibe was configured to shake vertically and use a 9 s sweep spanning frequencies from 20 to 500 Hz. The record is dominated by reflected arrivals, most of which are primary *S*-wave reflections based on their large normal moveouts (representing very low velocities). Prominent *P*-wave and *PS*-wave reflections from bedrock are also labelled.

Fig. 4 shows *PP* and *SS* seismic reflection sections (the latter with two different filters) acquired by operating the Microvibe and landstreamer as described above, at 3 m intervals along a line on asphalt that ran parallel to the seismoelectric spread and extended 180 m further south (Fig. 1). Both sections were generated using vertical component records. The two processing flows consisted of bandpass filtering, trace normalization, surgical muting of noise, semblance-based velocity analysis, normal moveout correction for either *P* or *S*-wave reflections, common midpoint stacking, and final bandpass filtering. An *S*-wave velocity depth section, generated by interpolating the interval velocities derived from stacking velocity analyses, is also shown. The section reveals a predominantly 1-D velocity structure in reasonable agreement with that measured in the borehole BH-NRC-MO. *S*-wave velocities increase significantly below the 18.5 m probed in that borehole as would be expected given a change from clay/silt sediments to diamicton/glacial till at 18.8 depth.

Approximate depth scales through the overburden are superimposed on the seismic sections. For the *SS* sections, two-way traveltimes were converted to depths using the borehole *S*-wave average velocity profile (Fig. 2), extrapolated below 18.5 m with the aid of the *S*-wave interval velocity depth section. For the *P*-wave section, we used a velocity model based on seismic refraction analyses presented in Section 4.3.1 below.

The *PP* and *SS* sections both show a package of strong reflections starting at approximately 23 m depth. These are interpreted to come from the bedrock surface and either shallow bedrock layers or peg-leg multiples generated by reverberation within the diamicton. The *PP* section shows a weaker coherent reflection at ∼18 m depth, inferred to be coming from the base of the Leda Clay or top of the diamicton. The higher resolution *SS* sections show additional detail at shallower depths. In particular, the high porosity/high clay content layer observed between 7 and 13.5 m depth in the borehole appears to be seismically transparent compared to the siltier, lower porosity layers enclosing it. We observe a clear *S*-wave reflection at the base of the high porosity layer at ∼13.5 m depth, associated with the abrupt increase in *S*-wave velocity found there in the borehole velocity log (Fig. 2). The overlying unit (<7 m depth), with its more variable porosity profile, exhibits multiple coherent reflectors.

3.2 Electrical resistivity structure

While the geotechnical properties and shear wave velocities of the Champlain Sea sediments in our study area were well characterized prior to our study in May 2011, this was not the case for the sediments' electrical properties. To support the analysis of seismoelectric phenomena, we therefore acquired an ERT profile (Fig. 1).

Using an *IRIS Syscal Pro* electrical imaging system with 24 electrodes at 5 m intervals, we adopted the *Wenner* four-electrode array known for its favourable signal strength and ability to resolve horizontal layering. Systematic acquisition errors were quantified by consideration of both measurement repeatability and reciprocity (Thompson *et al.* 2012) where the latter is the best error indicator (Binley *et al.* 1995). All resistivity measurements were highly repeatable and reproducible, characterized by an average standard deviation of 0.05 Ωm and a maximum of 0.28 Ωm, and thus all resistivity data were retained for inversion. The data were inverted using the DCIP2D algorithm (Oldenburg & Li 1994; Oldenburg & Li 1999) with a default Chi-factor to obtain smoothly varying 2-D models of bulk resistivity.

The ERT model exhibits resistivities ranging from 6 to 86 Ωm. Resistivities in excess of 20 Ωm, restricted to the uppermost few metres of the subsurface (Fig. 5), are interpreted to be indicative

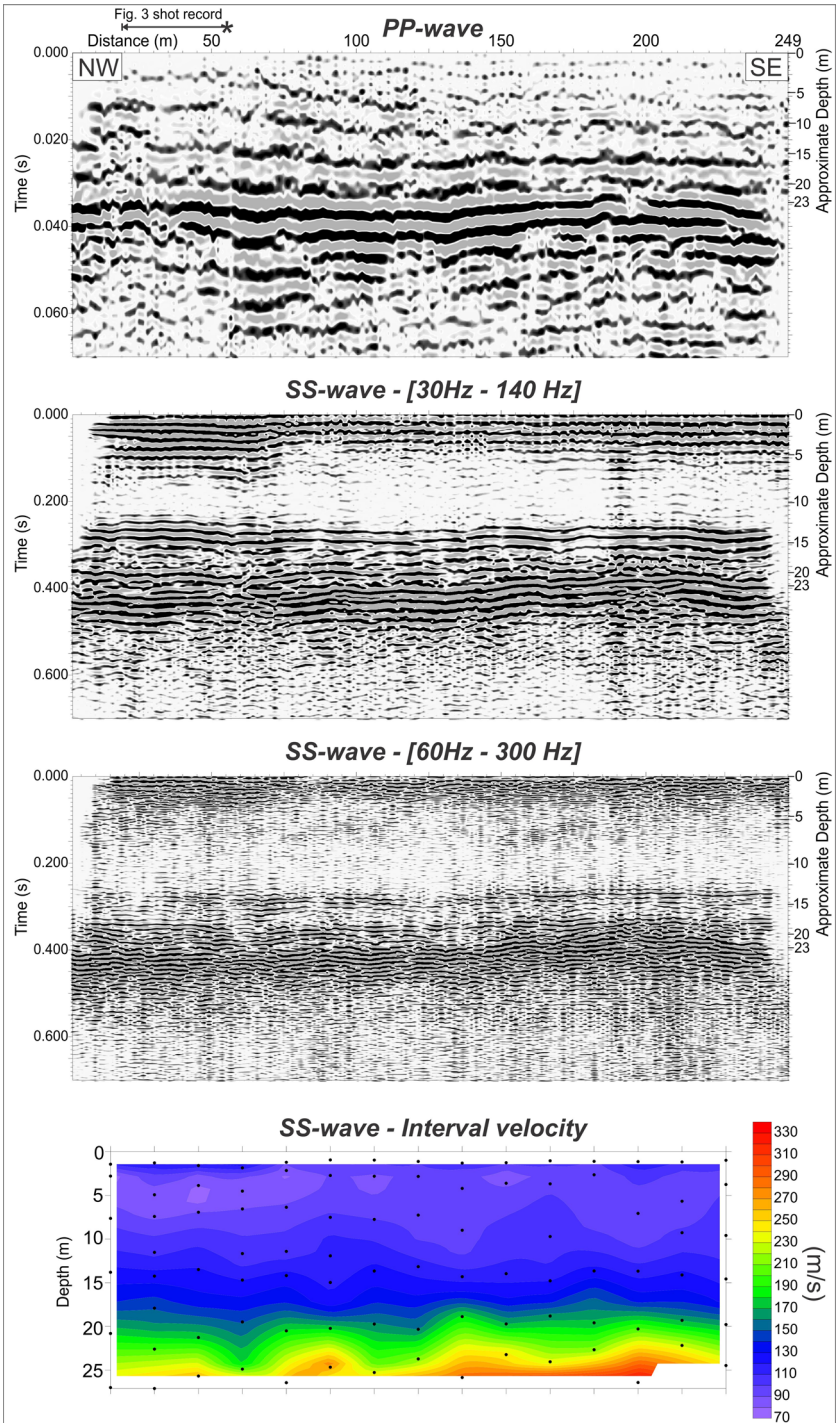

Figure 4. *PP* and *SS* seismic sections acquired using the portable Microvibe source and vertical component data from 24 geophones mounted on a landstreamer. The lowermost panel shows a depth section of *S*-wave interval velocities estimated from semblance-based velocity analyses on the pre-stack *SS* reflections. Location of the shot record in Fig. 3 is shown on the distance axis of the uppermost plot.

of the overconsolidated surface crust. We interpret the laterally heterogeneous nature of the uppermost layer to be a consequence of previous intrusive site activities, including the presence of patches of buried asphalt and the possible presence of buried drainage culverts or manholes that were occasionally observed at the ground surface. Below this layer, a gradual decrease in resistivity correlates with increasing clay content observed in the borehole (Fig. 2) to a depth of approximately 7 m. The layer of elevated clay content and porosity/water content between 7 and 13.5 m depth correlates with a region of low and relatively uniform electrical resistivity ($<$10 Ωm), below which the resistivities tend to increase again. We are uncertain of the origin of the near-vertical high resistivity anomaly spanning all depths between the 35 and 42 m marks of the profile. The laterally constrained nature of this anomaly is suggestive of a back-filled cavity or vertical shaft, although it might alternatively be an artefact associated with an off-line feature.

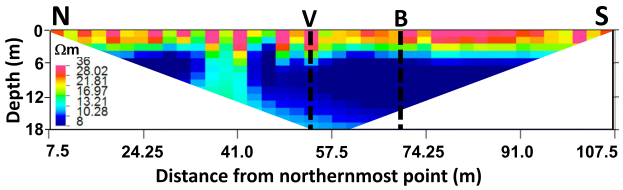

Figure 5. Resistivity section of the study site, based on a 2-D ERT survey acquired with an electrode spacing of 5 m. The dashed lines show the midpoints of the buffalo gun (B) and vibroseis (V) supergathers, as illustrated along with the ERT survey line in Fig. 1.

Finally, we note that although the lowermost layer of sediment, below 13.5 m depth has reduced clay and water contents, similar to those observed above 7 m, it is not characterized by similarly high resistivities in the subsurface model. This may be a consequence of reduced spatial resolution with depth.

4 SEISMOELECTRIC FIELD MEASUREMENTS

4.1 Seismoelectric data acquisition

Seismoelectric data were acquired using an array of 24 grounded dipole antennas, 4.5 m long, arranged end-to-end along the line used for the ERT survey (Fig. 1). An orthogonal pair of remote dipoles was used to measure ambient noise 100 m north of the northern end of the array. Each grounded dipole consisted of a pair of stainless steel stakes inserted approximately 30 cm into the ground and connected to a custom-built battery-powered differential amplifier providing signal buffering, a gain of 10, and a bandwidth of ∼0.4 Hz–20 kHz (Kepic & Butler 2002). The preamplifier outputs were connected to 12-channel seismic cables which were in turn connected to three 12-channel Geometrics Geode seismographs.

Our seismic sources included an in-hole shotgun and a mid-sized truck-mounted vibrator—the IVI Minivib producing 10 000 lb peak force (much larger than the Microvibe source discussed above). The Minivib was configured to vibrate the ground vertically using tapered 6 second sweeps from 20 to 350 Hz. A time-zero signal from the vibroseis controller triggered the seismographs. The shotgun used relatively large (8 gauge, 500 grain) black powder blank shells. It was inserted into holes augered to a depth of approximately 1 m, topped up with water. A custom-made piezoelectric transducer, mounted on the gun handle provided a 'clean' trigger that did not leak into the seismoelectric channels (Butler *et al.* 2007).

The Minivib was rolled through the spread of dipole receivers at 1.5 m intervals, offset laterally approximately 2–3 m from the line of electrodes to facilitate vibroseis deployment on the pavement. The shotgun source was deployed at just three shotpoints, set 1.5 m apart in a 4.5 m gap created by disconnecting one of the central dipoles and adding it to one end of the spread. By appropriate shot placement (see Kepic & Rosid 2004 or Dupuis *et al.* 2007) this allowed us to combine three adjacent 24-channel shot gathers having 4.5 m trace spacing into a single composite shot gather or supergather having 72 traces at 1.5 m spacing, thereby improving our ability to sample the seismoelectric wavefield and discriminate between arrivals based on their moveout characteristics. For supergather plotting and AVO analyses, shot-dipole offsets were taken as distances from shotpoint to the middle of each 4.5 m dipole.

Corresponding seismic supergathers were collected by disconnecting the dipoles, placing a vertical 28 Hz geophone at each electrode and re-occupying all shotpoints previously used for the seismoelectric measurements. Geophones were not deployed at the time of seismoelectric data acquisition so as to guard against any possibility of cross-talk.

4.2 Seismoelectric data processing

The objective of the seismoelectric field trial was to determine whether interfacial effects could be detected in an electrically conductive, low permeability environment. Therefore, processing steps were focussed on the improvement of signal-to-noise (S/N) ratios in shot and receiver supergathers, providing the dense trace spacing and wide range of source-receiver offsets required to reveal the diagnostic moveout characteristics of different seismoelectric arrivals.

Noise was dominated by powerline harmonic interference at 60 Hz and its harmonics. We also observed some broader band noise, suspected to be AM radio pickup, which can be inadvertently demodulated in seismoelectric preamplifiers and/or seismograph amplifiers leading to noise in the audio frequency band (Kepic & Butler 2002; Butler *et al.* 2007). Harmonic noise subtraction (Butler & Russell 2003) was very helpful although its effectiveness was limited by instability of the powerline source(s). The effects of this non-stationarity were mitigated by acquiring and processing shot records individually prior to stacking (Butler 2001), and by use of remote reference subtraction since the instabilities were largely correlated over all of the dipoles. In some cases, conventional notch filtering was beneficial to achieve further reduction in the amplitude of residual harmonic noise.

Powerline harmonic noise estimates were made using the pre-trigger portion of records acquired using the buffalo gun, but in the case of the vibroseis data, pre-trigger data could not be recorded. Harmonic noise estimates were made on the vibroseis records after they had been correlated with their pilot traces, as we found there was no improvement in applying harmonic subtraction prior to correlation.

S/N ratios were also improved by stacking processed records from multiple shots at the same location and by stacking traces with common offsets from multiple closely spaced shotpoints as discussed further below. Shot records found to be exceptionally noisy after processing were manually excluded. In the case of the vibroseis data, slightly improved stacks were obtained using a diversity stack algorithm (Klemperer 1987) which automatically weighted the traces contributing to a stack inversely to their average power (amplitude squared) in 100 ms windows; stacked traces were normalized by the sum of the trace weights in each time window. In this way, the impact of traces exhibiting random bursts of noise was reduced automatically.

4.3 Results of the seismoelectric field trial

We present below three supergathers—two composite shot gathers and one composite receiver gather—comparing seismic and seismoelectric arrivals acquired using the two different seismic sources.

4.3.1 Shotgun source

Figs 6(a) and (b) show shotgun seismic and seismoelectric supergathers assembled from three shotpoints distributed across a distance of 3 m centred at point B in Fig. 1. The seismic supergather has greater offsets as we had 36 geophones available as opposed to only 24 grounded dipoles. Up to four shotgun blasts were stacked at

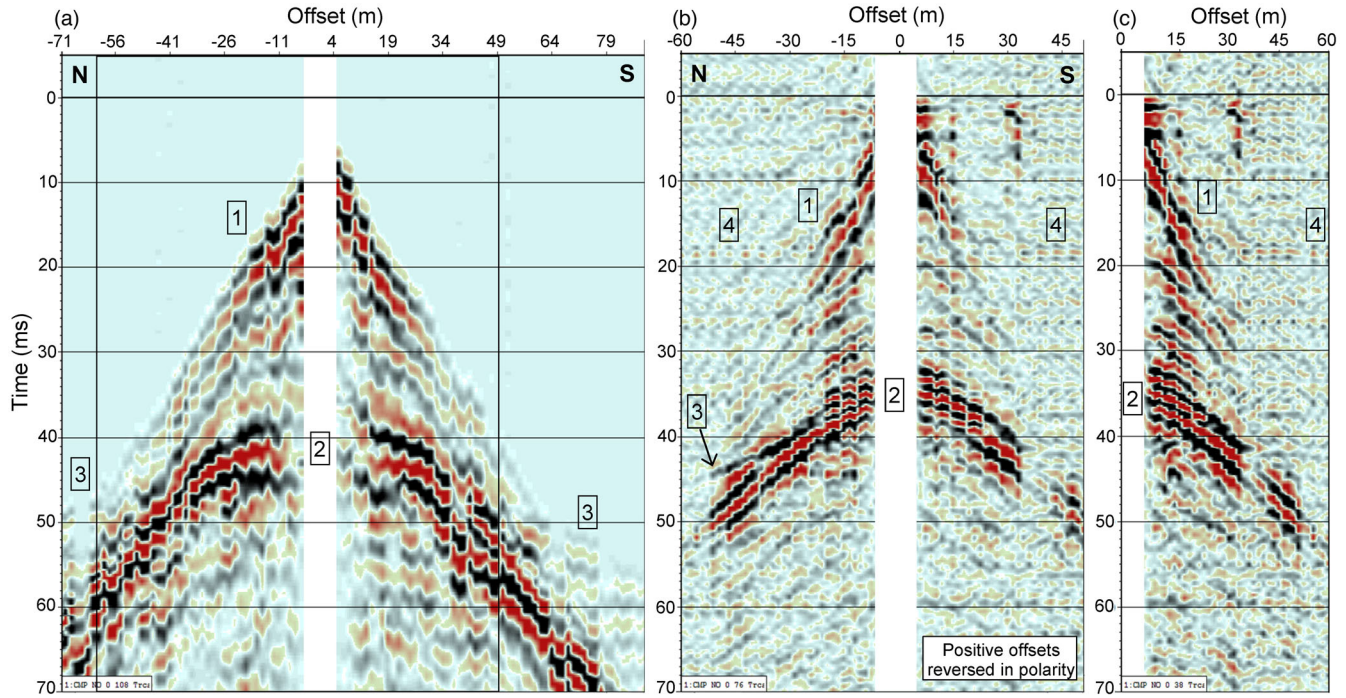

Figure 6. Comparison of very high resolution seismic (a) and seismoelectric (b) composite shot gathers acquired using a shotgun seismic source and gently bandpass filtered from 200 to 800 Hz. Traces within each record are plotted at true relative amplitudes. Offsets range from −60 to +51 m (−71 to +88 m for the seismic) with a trace spacing of 1.5 m. Panel (c) is a single-sided shot composite shot gather formed by stacking traces at corresponding positive and negative offsets in (b). Numbers indicate (1) direct *P*-wave, (2) *P*-wave reflected from bedrock, (3) *P*-wave refraction from bedrock and (4) a possible interfacial seismoelectric effect from bedrock. Note the broader bandwidth and earlier arrival of the bedrock reflection in the seismoelectric record.

each shotpoint in the case of the seismoelectric data. Both data sets have been bandpass filtered using a gentle (12 dB/octave) causal 200–800 Hz Butterworth filter which attenuated low frequencies and thereby improved spectral balancing.

To begin, it is instructive to consider information contained in the seismic supergather alone. Analysis of the first seismic arrivals (see Fig. 7), accounting for the 1 m shot depth, reveals that they exhibit apparent *P*-wave velocity of ∼700 m s^{-1} within 3 m of the shotpoint, increasing to ∼1420 m s^{-1} at intermediate offsets and 3950 m s^{-1} at offsets greater than 63 m. Simple seismic refraction interpretation of those observations in terms of a horizontally layered model suggests the presence of a thin partially saturated upper layer having a thickness of 1.4 m, overlying water-saturated sediments, with bedrock at a depth of approximately 23 m. The second layer's *P*-wave velocity estimate of 1420 m s^{-1} is consistent with the hyperbolic normal moveout of the reflection from the top of diamicton or bedrock labelled (2) in Fig. 6(a).

Three features are immediately apparent on comparing the seismic and seismoelectric supergathers in Fig. 6. Superficially, the seismoelectric record appears to be dominated by coseismic effects, that is, by arrivals exhibiting moveout patterns very similar to those exhibited by the seismic arrivals. We can identify a direct *P*-wave (labelled 1), a *P*-wave refracted from the top of bedrock (3), and a package of closely spaced *P*-wave reflections interpreted to be from the top of diamicton and bedrock (2). Second, the seismoelectric data have much broader bandwidth, exhibiting dominant frequencies as high as 600 Hz compared to 300 Hz or less in the seismic data. Third, the coherency of reflected arrivals is better in the seismoelectric record. The presence of two or three overlapping reflections in the package labelled (3), and of additional shallower reflections, is more evident in the seismoelectric data because of its higher bandwidth and superior coherency.

We note also that the bedrock reflection (3) arrives approximately 6 ms earlier in the seismoelectric record compared to the seismic record. The fact that the bedrock reflection is detected at surface by electric field sensors well before it is detected by geophones indicates that the reflected seismic wave is giving rise to a propagating electric field pulse some distance below the surface. Unlike the seismic wave, this electric field is not significantly attenuated or differentially delayed by propagation through the low *P*-wave velocity 'weathered layer' at surface, thereby explaining its broader bandwidth and superior coherency. If we consider that the electromagnetic traveltime is negligible relative to the seismic (*P*-wave) traveltime, then the electric field must be emanating from whatever depth the returning bedrock reflection has reached 6 ms before its arrival at surface. Considering the *P*-wave velocity model in Fig. 7, 6 ms corresponds to a depth of approximately 7 m. Thus it would appear that the seismoelectric response (3) is generated at the top of the layer of anomalously high porosity, clay content and electrical conductivity found between 7 and 13.5 m depth. This represents a new type of seismoelectric phenomenon, not previously documented in field or lab experiments (Butler *et al.* 2013, 2014) but recently predicted in full waveform seismoelectric modelling by Ren *et al.* (2015); it is generated at an interface (like an interfacial seismoelectric effect), but exhibits the same moveout characteristics as the seismic wave (like a coseismic seismoelectric effect). We return to a discussion of this phenomenon in the Discussion below.

True interfacial seismoelectric effects are expected to exhibit (i) negligible moveout with offset, (ii) polarity inversion on opposite sides of the shotpoint, and (iii) amplitude variation with offset similar to that expected for a vertical dipole situated on the interface

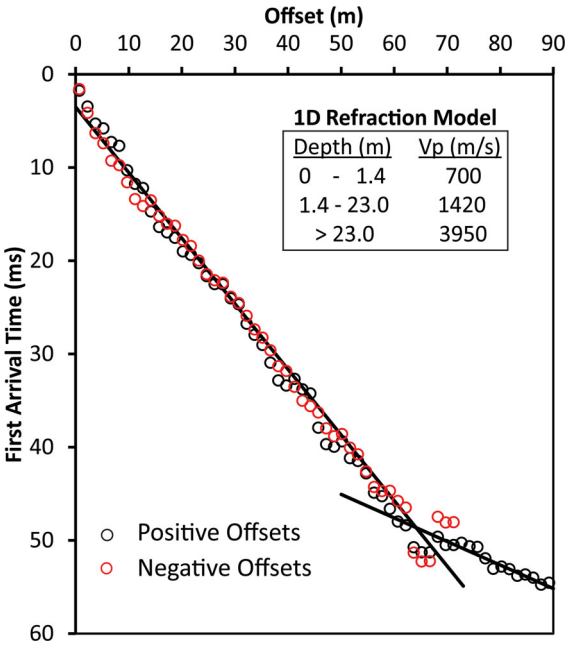

Figure 7. Analysis of first arrivals in the shotgun seismic supergather in terms of a *P*-wave velocity model for the site consisting of three horizontal layers. Critically refracted arrival times shown here have been increased by 1.4 ms to correct for the fact that the shotgun shell was detonated at a depth of 1 m in an upper layer.

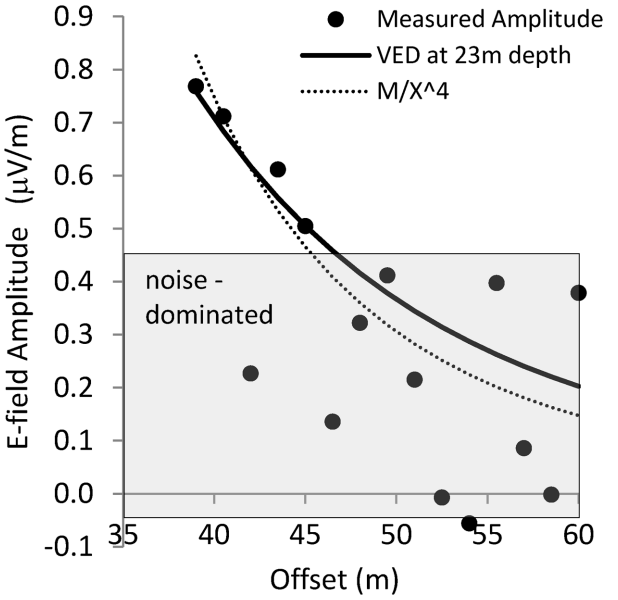

Figure 8. Amplitude of the possible interfacial seismoelectric conversion from top of bedrock (event (4) in Fig. 6c) plotted as a function of shot-receiver offset. The solid curve shows the rate of amplitude decay that would be expected for vertical dipole source situated at the top of bedrock 23 m below surface; at these intermediate offsets the rate of decay is nearly indistinguishable from $1/x^3$ dependence, x being shot-receiver offset. For comparison, the dotted line shows the $1/x^4$ amplitude dependence that would be expected at offsets much greater than the depth to the responsible interface.

directly beneath the shot. For ease of visual pattern recognition, the polarities of seismoelectric traces to the south of the shot have been reversed in Fig. 6(b) so that any valid interfacial effects should appear to have the same polarity across the entire record. In contrast, ambient noise from distant sources should exhibit opposite polarities on opposite sides of the shot in this presentation. In Fig. 6(c), traces at corresponding offsets to the north and south have been added together and plotted as a one-sided supergather. Under ideal conditions in a horizontally layered earth with no lateral heterogeneity, this 'flip and stack' procedure would have the effect of doubling the amplitudes any interfacial effects and cancelling noise from distant sources.

The event labelled (4) in Figs 6(b) and (c) exhibits characteristics that would be expected for an interfacial seismoelectric conversion occurring at the top of bedrock, including an arrival time consistent with the one-way *P*-wave traveltime to bedrock. Fig. 8 shows how the amplitude of this event, obscured by coseismic effects close to the shotpoint, varies between offsets of 39 and 60 m in Fig. 6(c). The maximum potential difference was approximately 4 μV over a 4.5 m long dipole, representing an electric field amplitude of 0.8 μV m^{-1}. This is small compared to amplitudes of up to 5 μV m^{-1} for coseismic effects in the record, and to noise levels of 175–1150 μV m^{-1} in the raw shot records. The amplitude measurements in Fig. 8 generally decrease with offset x over a distance of several metres but become noise-dominated beyond 45 m offset that where amplitudes drop below ~0.4 μV m^{-1}. The rate of amplitude decay observed where the signal is sufficiently strong, is comparable to what would be predicted for a vertical electric dipole source located at the top of bedrock ~23 m below surface (cf. Butler *et al.* 1996; Garambois & Dietrich 2002; Dupuis *et al.* 2007). This provides further evidence that event (4) may be an interfacial effect generated at the top of bedrock, although it must be acknowledged that the interpretation is speculative given the event's low S/N ratio.

4.4 Seismoelectric records acquired with a vibroseis source

Fig. 9 presents seismic and seismoelectric supergathers assembled from vibroseis records acquired with the Minivib source at 12 adjacent source points located 1.5 m apart and centred at point V in Fig. 1. The source effort in the seismoelectric case was very high—each trace representing a stack up of to 60 vibroseis sweeps (i.e. 15 vibroseis sweeps at each source point multiplied by four because every third source point recorded the same trace offsets). The records have again been gently highpass filtered with a corner frequency of 200 Hz. Note however that the 112 ms record length used in Fig. 9 is much greater than the 70 ms record length used in Fig. 6. It is readily apparent that the buffalo gun source provided much higher resolution data than the Minivib in this environment.

The seismic supergather is shown with and without the application of automatic gain control (AGC) scaling prior to vibroseis correlation in Figs 9(a) and (b) respectively. Pre-correlation AGC helps to compensate for frequency-dependent attenuation of the vibroseis sweep signal in the uncorrelated seismic traces, thereby increasing the bandwidth of the correlated seismic data. Unfortunately, this approach is not applicable to the seismoelectric data because the amplitude of each uncorrelated trace is dominated by powerline and other noise which is, to first order, constant over the length of the record.

Comparing the seismic and seismoelectric supergathers processed without AGC, in Figs 9(b) and (c), it is clear that they differ from each other in the same ways as were evident in the buffalo gun comparison. In particular, the prominent reflection hyperbola (with a zero-offset arrival time just before 40 ms) has broader bandwidth and is more symmetrical and laterally coherent in the seismoelectric record. Furthermore, it arrives earlier in the seismoelectric record although the difference in arrival time is more obvious and easier to measure in the buffalo gun data (Fig. 6) which has much broader

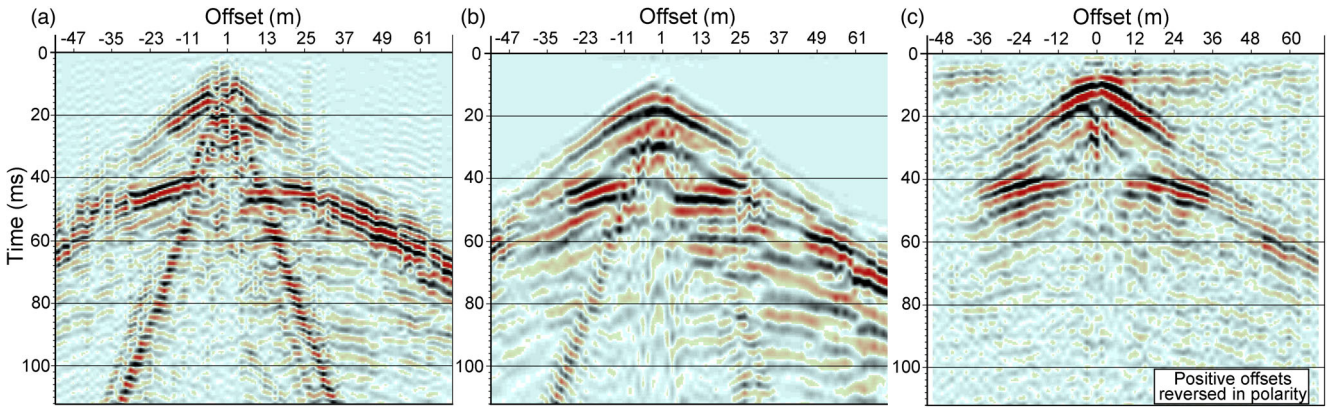

Figure 9. Comparison of seismic (a, b) and seismoelectric (c) composite shot gathers acquired using the Minivib vibroseis source with a 20–350 Hz sweep, subsequently highpass filtered at 200 Hz. Trace amplitudes have been normalized by their RMS values. Offsets range from −51 to +72 m with a trace spacing of 1.5 m. Seismic results (a) and (b) differ in that 1 s AGC scaling was applied to (a) prior to vibroseis correlation in order to counteract high frequency absorption. Comparing (b) and (c) which were processed in the same way, it is again evident that the *P*-wave reflection from bedrock is detected sooner and exhibits broader bandwidth in the seismoelectric record.

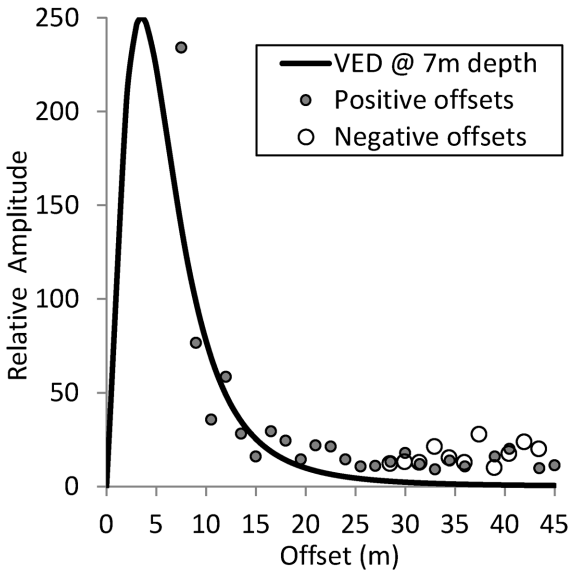

Figure 10. Amplitude versus offset (AVO) behaviour of an early electrical event appearing at approximately 8 ms and exhibiting near-zero moveout in the composite vibroseis shot gather (Fig. 9). Solid line shows the AVO profile that would be expected for a vertical electric dipole source at 7 m depth, having its dipole moment scaled to fit the near-offset measurements. There is reasonable agreement for near to intermediate positive offsets but the lack of signal decay beyond 20 m is suggestive of noise.

frequency content. Note also that the air wave visible in the seismic record is not present in the seismoelectric data.

With respect to possible interfacial seismoelectric effects, the Minivib record in Fig. 9(c) exhibits two arrivals with near-zero moveout on the right hand side of the source, appearing at times of 6–8 ms and 20–22 ms. At first glance, these would appear to be good candidates for interfacial effects generated by *P*-waves impinging on the top of the high porosity clay-rich layer and on the top of diamicton or bedrock. In both cases however, the signals are poorly developed to the left of the source. The origin of the events is therefore ambiguous. Amplitudes for the event at 20–22 ms are barely above the noise level, but the 6–8 ms event is sufficiently strong to merit investigation of its AVO behaviour. As shown in Fig. 10, the amplitudes measured at near to intermediate positive offsets of 7.5 to 20 m decay approximately as would be expected for a vertical dipole source positioned at the top of the porous clay-rich layer at 7 m depth. However, at larger offsets from 20 to 45 m where modelled amplitudes decay by a factor of 20, measured amplitudes remain nearly constant, suggestive of some sort of coherent noise. These AVO observations, together with the lack of signal at near to intermediate negative offsets, and the asymmetrically dipping appearance of the arrival at long offsets leads us to conclude that the early arrival may be an interfacial effect that has been overprinted by some kind of early-time acquisition artefact related to the Minivib source.

The vibroseis records presented in Fig. 11 are five times longer than those shown in Fig. 9, and have been bandpass filtered to retain the relatively low frequencies that dominate the *PS*/*SP* and *SS* reflections arriving very late in time. Furthermore, unlike the composite shot gathers considered above, Fig. 11 is composed of receiver gathers. Fig. 11(a) shows all seismic traces recorded by one geophone near the middle of the seismoelectric array in response to operation of the Minivib source at 57 different source points. Fig. 11(b) is a composite receiver gather of all the traces recorded from the same source points by the two dipole receivers adjacent to that geophone location.

Receiver gathers were used in this case because it allowed us to demonstrate the arrival time versus offset (i.e. moveout) behaviour of seismoelectric arrivals using a pair of dipole antenna receivers that exhibited relatively good S/N ratios. The one drawback of using receiver gathers is that the arrival time of an interfacial seismoelectric conversion depends on the seismic traveltime from source point to the interface which may differ for every trace; thus an interfacial effect will not necessarily appear as an event with negligible moveout as it does on a shot record.

The point of Fig. 11 is primarily to highlight the abundance of coseismic or apparently coseismic seismoelectric effects that were observed at this site in association with both primary and mode-converted seismic reflections. Seismoelectric arrivals are now evident for *PS*/*SP* and *SS* reflections in addition to the *PP* bedrock reflection. Exceptionally slow surface wave arrivals (absent from previous plots that had been highpass filtered) can also be seen, overprinting the shallowest *SS* reflections, with so much moveout that they are heavily aliased. As before the reflected seismic arrivals appear to follow their seismoelectric equivalents, although visually

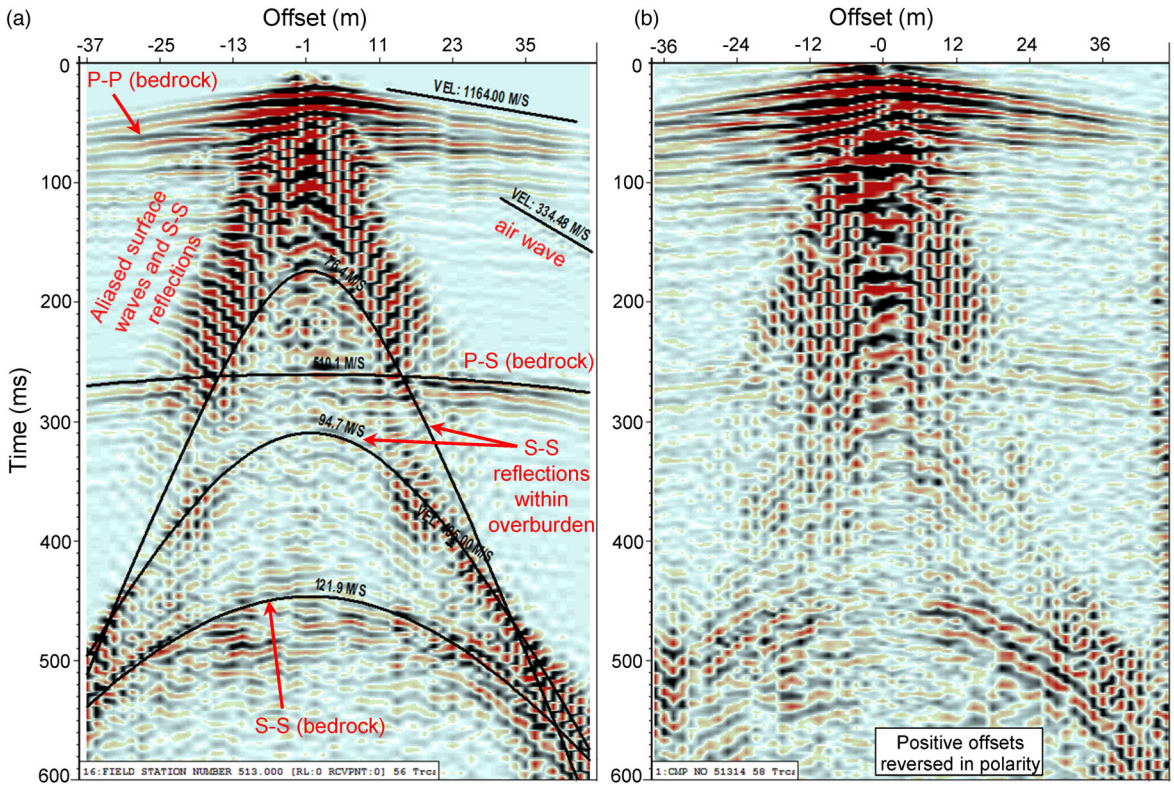

Figure 11. Comparison of long, low frequency seismic (a) and seismoelectric (b) receiver gathers acquired using the Minivib vibroseis source with a 20–350 Hz sweep, subsequently bandpass filtered from 15 to 150 Hz. Time-varying gain, ramping up exponentially from 0 to 12 dB (1 to 4 times), has been applied over the first 200 ms. Otherwise, no trace scaling or normalization has been applied. These records are five times longer than those shown in Fig. 9, in order to reveal the arrival of *PS*/*SP* and *SS* reflections in both the seismic and the seismoelectric data. Offsets range from −37 to +47 m with a trace spacing of 1.5 m.

the difference is less obvious owing to these lower frequencies and longer records.

5 DISCUSSION

The Minivib source worked well for seismoelectric data acquisition. The ease with which recordings could be repeated at the same shotpoint was an advantage over the buffalo gun, especially given the value of being able to implement 'smart stacking' techniques such as the diversity stack to reduce the influence of noise bursts during post-processing. The one major advantage of the buffalo gun source was its significantly greater bandwidth. At this site, underlain by Leda Clay sediments with exceptionally low seismic absorption characteristics, the seismoelectric records benefited from the higher bandwidth of the buffalo gun source even more so than the seismic records.

Two of the seismoelectric modes observed in this study—namely the coseismic effect accompanying the arrival of direct *P*-waves at each dipole antenna, and the possible interfacial conversions generated by *P*-waves—have been well documented by previous experimental and theoretical studies. The possible interfacial effect identified in the buffalo gun supergather, exhibiting a peak amplitude of approximately 0.8 μV m^{-1}, is associated with a strong seismic impedance contrast, at the clay/diamicton or diamicton/bedrock contact, as has been the case in previous reports. However, it differs from previous observations in that it was detected through an electrically conductive (8–15 Ω m) clay/silt cover. In contrast, the interface at 7 m depth, which gives rise to a possible interfacial effect in the vibroseis-source seismoelectric supergather is not a significant impedance contrast according to the *P* and *S*-wave reflection sections in Fig. 4; it is instead characterized by contrasts in porosity and electrical conductivity according to the geotechnical logs (Fig. 2) and the ERT section (Fig. 5).

It is counterintuitive that the bedrock interfacial effect was not clear in the vibroseis record while the porous layer interfacial effect did not stand out in the shotgun data. Although the two supergathers were centred 20 m apart, seismic sections from the site (Fig. 4) led us to expect a high level of lateral continuity. The fact that the vibroseis data were averaged over a larger number of shotpoints (12 shotpoints spanning 16.5 m versus 3 shotpoints spanning 3 m for the shotgun source) could be relevant; this had the desired effect of increasing the S/N ratios for quasi-coseismic arrivals, but would have required the top of bedrock to be very flat (or more precisely, lateral consistency in *P*-wave traveltime to bedrock) for enhancement of its interfacial effect. Apart from that, it must be acknowledged that the signal to noise levels for the interfacial effects were simply very low in both records.

The supergathers also show seismoelectric events mimicking the arrival time versus offset patterns (i.e. moveout patterns) of *PP*, *PS*/*SP* and *SS* reflections returning to surface. Superficially, these seismoelectric arrivals could be attributed to coseismic effects associated with the seismic reflections. Indeed, coseismic effects associated with the arrival of reflected *P*-waves at antennas on surface appear in full waveform modelling (see, for example, fig. 3 in Haartsen & Pride 1997). While that explanation is probably partly correct, it fails to account for three observations in these field data: (i) reflection events in the seismoelectric records arrive several ms ahead of their arrival in corresponding seismic records; (ii) the

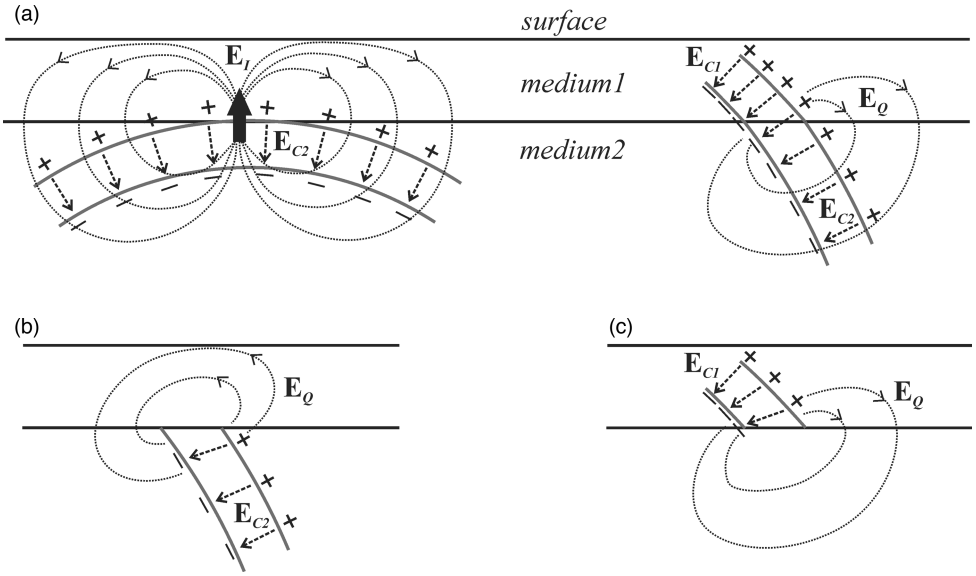

Figure 12. (a) Conceptual model for three types of seismoelectric fields (represented as dashed lines) expected to be associated with an upward-travelling *P*-wave in the vicinity of a near-surface boundary, including an interfacial effect $\mathbf{E}_I$, two coseismic effects $\mathbf{E}_{C1}$ and $\mathbf{E}_{C2}$, and a quasi-coseismic effect $\mathbf{E}_Q$. Parts (b) and (c) show end-member quasi-coseismic effects to be expected in cases where there is negligible electrokinetic charge separation in one layer or the other.

reflection events appear more coherent and have broader frequency content in the seismoelectric records, and (iii) *S*-waves are not expected to carry coseismic electric fields.

A conceptual model that can account for these three observations, in terms of a quasi-coseismic effect, is presented in Fig. 12. The model considers the fundamental source of seismoelectric fields to be the charge separation that occurs between the compressions and rarefactions of a *P*-wave as it travels through a water-bearing porous medium. Following the approach in Butler *et al*. (1996), this charge separation is represented in a simplified way using charged seismic wave fronts, separated by one-half of the dominant seismic wavelength. Within any homogenous layer, this gives rise to coseismic electric fields ($\mathbf{E}_C$) that are trapped within the *P*-wave. In Fig. 12(a), we show how an upward-travelling, spherically spreading *P*-wave, such as one reflected from depth, should be expected to give rise to two additional seismoelectric modes as it crosses a boundary. The first of these two boundary modes is the familiar interfacial seismoelectric conversion, giving rise to an electric field pattern $\mathbf{E}_I$ similar to that produced by a vertical electric dipole centred at the interface point first reached by the *P*-wave; the electric field radiates in all directions at the speed of an electromagnetic wave and should therefore be detected near-simultaneously at widely separated antennas although it's amplitude decays rapidly with offset. However, a second boundary mode—a quasi-coseismic effect denoted $\mathbf{E}_Q$ in the right-hand side of Fig. 12(a)—can also be expected to develop as the *P*-wave spreads out laterally along the interface. This effect had not been recognized in previous experimental investigations, although, in hindsight, it can be seen in at least two previous data sets, as discussed further below.

Coincidentally, quantitative modelling has very recently predicted the existence of this quasi-coseismic effect; Ren *et al*. (2015), apparently unaware of our experimental results (Butler *et al.* 2013, 2014) demonstrated that it should exist by considering the limiting case of an upward propagating elastic wave incident in water-saturated porous media incident on an interface with an overlying solid layer (representing a completely dry surficial layer, therefore incapable of supporting coseismic effects). Their full waveform seismoelectric modelling predicted that evanescent EM waves should be induced by *P*- and *S*-waves with angles of incidence greater than the very small critical angles determined by the ratios of their velocities to the EM wave velocity. Physically, they explained that the effect should be expected because of the requirement for continuity of the component of the electric field parallel to the interface. In the paragraphs below, we elaborate on our charged wave-front conceptual model for this effect, and consider the conditions under which it may be expected to appear.

Referring again to Fig. 12(a), the quasi-coseismic effect $\mathbf{E}_Q$, like the interfacial effect $\mathbf{E}_I$, can be expected to radiate beyond the confines of the *P*-wave as a consequence of disruption of the spherical symmetry of the charged seismic wave fronts at the boundary. This disruption can be brought about by a change in *P*-wave velocity (causing wave-front refraction and a change in dominant wavelength), and/or by changes in the physical properties that control the charge separations, and hence the coseismic fields $\mathbf{E}_{C1}$ and $\mathbf{E}_{C2}$, that develop in the two media above and below the interface. The right-hand side of Fig. 12(a) depicts the general case where the quasi-coseismic effect is expected to leak out of the propagating *P*-wave as a consequence of both a change in velocity and changes in the physical properties controlling charge densities in the peaks and troughs of the *P*-wave above and below the interface. The generation of reflected *P*-waves or of mode-converted poroelastic slow *P*-waves might also contribute to the source, although no attempt is made to incorporate them here.

Figs 12(b) and (c) show special cases of this model where the layer above or below the interface does not contain any electrokinetic charge separation: a completely dry surficial layer or a layer of water (such as a lake or ocean) for example. Alternatively, a situation like that depicted in Fig. 12(c) could arise where the upward travelling reflection is an *S*-wave which does not generate charge separation in the lower layer but is mode-converted to a *P*-wave inducing charge separation in the upper layer; this provides a possible explanation for the fact that *SS* reflections are observed in the seismoelectric record of Fig. 11. The two diagrams illustrate that, in these special cases, the quasi-coseismic field detectable at the earth's surface

is conceptually similar to the fringing field detectable outside the edges of a parallel plate capacitor.

The physical properties that directly influence the strengths of coseismic fields on either side of an interface include the electrical conductivities of the two formations, as well as their electrokinetic streaming current coupling coefficients, and poroelastic moduli that control the relative fluid flow induced within a *P*-wave (see, e.g. Neev & Yeatts 1989; Pride & Haartsen 1996; Garambois & Dietrich 2001; Dupuis & Butler 2006). It is clear, therefore, that the mismatch in the coseismic effects between two adjacent formations may arise from a wide variety of physical property contrasts. Given the direct (inverse) dependence on electrical conductivity, and the wide range of conductivities between geological formations, contrasts in electrical conductivity could be a common source of the quasi-coseismic effects. The strong contrast in *P*-wave velocity at the base of the seismic weathered layer is another likely source—as a consequence of wave-front refraction alone.

The quasi-coseismic effect observed in this field trial originated approximately 7 m below surface. Seismic refraction analysis (Fig. 7) shows no evidence of a change in *P*-wave velocity at that depth. Thus, upward travelling *P*-waves would undergo negligible wave-front bending at this interface and must give rise to quasi-coseismic effects due to a change in the strength of the coseismic effect alone. This change is likely a consequence of the drop in porosity (Fig. 2) and increase in electrical resistivity (Fig. 5) encountered in propagating upward across that interface. For upward travelling *S*-waves, the near-coincident 20 per cent drop in *S*-wave velocity (from 100 to 80 m s^{-1}, Fig. 2) could give rise to mode-converted *P*-waves at the interface and a quasi-coseismic effect like that shown in Fig. 12(c) as discussed above.

One curious observation is that the quasi-coseismic seismoelectric effects measured in this case were much stronger than any interfacial seismoelectric conversions produced at the same interface—by either downgoing or upgoing *P*- or *S*-waves. It would be interesting to model the expected amplitudes of interfacial versus quasi-coseismic effects, and their dependence on interface depth and seismic wavelength using the model of Ren *et al.* (2015) and the abundant physical property data available for this site.

Although the conceptual model (Fig. 12) proposed for the quasi-coseismic effect is new, there is evidence that the effect itself has been observed in previous field studies. For example, Martner & Sparks (1959) reported on seismoelectric pulses generated at the base of the weathered layer in various parts of Oklahoma by *P*-waves travelling upward from explosive charges in shot holes. In some cases, they observed that the seismoelectric pulse originated directly above the shot location and was detected simultaneously by widely spaced dipole antennas on surface—suggestive of a true interfacial effect emanating from a seismoelectric Fresnel zone (Garambois & Dietrich 2002) on the interface centred directly above the shot location. More commonly, however, Martner & Sparks (1959) observed clear seismoelectric pulses coinciding with the *P*-wave arrival at the base of the weathered layer beneath each receiving antenna. These seismoelectric arrivals preceded the seismic arrivals at surface but exhibited very similar moveout patterns—diagnostic of quasi-coseismic effects.

Two other examples can be found in the results of field experiments conducted at Haney, BC, Canada as reported by Butler *et al.* (1996) and Russell *et al.* (1997). The focus in those experiments was on the identification of interfacial effects, distinguished by their simultaneous arrival across widely spaced dipole antennas. However, both reports also point out secondary seismoelectric arrivals that exhibit arrival times and seismic-like moveout patterns suggesting that they were generated at the road fill/glacial till contact beneath each dipole receiver.

In one sense, the quasi-coseismic interfacial effect, produced near the surface by returning *P* and *S*-wave reflections, constitutes another type of coherent noise in the search for true interfacial conversions from depth. On the other hand, it could prove useful in regions where it is measureable. Martner & Sparks (1959)—although silent on the mechanism and reliant on strong *P*-waves travelling upward directly from an explosive charge—had suggested that the phenomenon be used to calculate static corrections in support of seismic reflection surveys. Alternatively, in suitable areas, the effect could be used for recording seismic reflections directly with electric field sensors—offering improved bandwidth and coherency compared with surface seismic sensors that detect reflections only after they have experienced the absorption and differential delays associated with passage through the weathered layer. Lateral variations in the physical properties controlling coseismic effects above and below near-surface interfaces may also be detectable through their impact on the amplitude of this quasi-coseismic effect.

6 CONCLUSIONS

A field trial of surface seismoelectric surveying was carried out at a site where the upper 20 m of clay-rich sediments were very different from the porous, permeable sedimentary environments targeted in most previous seismoelectric field experiments. Very low seismic absorption and minimal surface wave interference, combined with multichannel recording over a wide range of offsets, made it possible to identify seismoelectric effects associated with an unusually rich near surface seismic wavefield. While the shotgun source yielded broader bandwidth data, the vibroseis source also performed well, generating clean seismoelectric records.

Possible interfacial seismoelectric effects emanating from the overburden/bedrock interface at ∼20 m depth and from the top of a highly porous and conductive layer at 7 m depth were identified. However, the most prominent seismoelectric arrivals were those observed to mimic the numerous direct and reflected body wave arrivals evident in the seismic records. The earlier arrival, broader bandwidth and superior coherency of the reflected arrivals in the seismoelectric records, compared to the seismic records, are all consistent with the generation of quasi-coseismic electric field responses by reflected *P* and *S* seismic waves impinging on the shallow 7 m deep boundary below each electric field receiver. These quasi-coseismic seismoelectric arrivals may be understood as evanescent seismoelectric effects of the type recently predicted by Ren *et al.* (2015). Their recognition at this site helps to explain the origin of similar effects reported in previous studies and will contribute to improved interpretation of seismoelectric records.

Given the well-characterized nature of this site, the high resolution observations of multimode seismoelectric arrivals may be particularly attractive for tests of full waveform modelling—aiming to reproduce the various seismoelectric modes and their relative amplitudes. In terms of practical applications, the field trial suggests that low power (shotgun) seismic sources may be adequate to generate measureable (∼1 μV m^{-1}) interfacial seismoelectric effects emanating from beneath 20 m of highly conductive clay. However, multichannel/multioffset recording is required to confidently differentiate such interfacial effects from larger coseismic or quasi-coseismic effects based on moveout and amplitude-

versus-offset criteria. The field trial also demonstrates that, where suitable shallow interfaces exist, electric field receivers on surface can yield dramatically higher resolution records of seismic reflections than can be obtained using surface seismic receivers.

ACKNOWLEDGEMENTS

The field study was supported by an NSERC Discovery Grant awarded to KEB. Our collaboration was made possible by a Harrison McCain Foundation Visiting Professorship award and an International Exchanges award from The Royal Society. We acknowledge Dr. Anton Kepic for design of the seismoelectric preamplifiers, and the Geophysical Inversion Facility of the University of British Columbia for making their DCIP2D inversion code available to us. We thank Timothy Cartwright, Kevin Brewer, Andrew Ringeri and Sally Reid for their assistance in the collection of the field data, and Heather Crow for preparing the geotechnical borehole log.

REFERENCES

Araji, A.H., Revil, A., Jardani, A., Minsley, B.J. & Karoulis, M., 2012. Imaging with cross-hole seismoelectric tomography, *Geophys. J. Int.,* **188**(3), 1285–1302.

Binley, A.M., Ramirez, A. & Daily, W., 1995. Regularised image reconstruction of noisy electrical resistance tomography data, in *Proceedings 4th Workshop of the European Concerted Action on Process Tomography*, pp. 401–410, Bergen.

Bordes, C., Jouniaux, L., Garambois, S., Dietrich, M., Pozzi, J.-P. & Gaffet, S., 2008. Evidence of the theoretically predicted seismo-magnetic conversion, *Geophys. J. Int.,* **174**(2), 489–504.

Bordes, C., Sénéchal, P., Barrière, J., Brito, D., Normandin, E. & Jougnot, D., 2015. Impact of water saturation on seismoelectric transfer functions: A laboratory study of coseismic phenomenon, *Geophys. J. Int.,* **200,** 1317–1335.

Bozozuk, M. & Leonards, G.A., 1972. The Gloucester test fill, in *Special Conference on Performance of Earth and Earth-Supported Structures*, ASCE, Purdue University, Layfayette, Indiana, Vol. 1, Part 1, pp. 333–349.

Butler, K.E., 1996. Seismoelectric effects of electrokinetic origin, *PhD thesis*, The University of British Columbia, Vancouver.

Butler, K.E., 2001. Comment on "Design of a Hum Filter for Suppressing Power-line Noise in Seismic Data" by J. Xia and R.D. Miller (J. Environmental and Engineering Geophysics, 5, 31–38), *J. Environ. Eng. Geophys.,* **6**(2), 103–104.

Butler, K.E. & Russell, R.D., 2003. Cancellation of multiple harmonic noise series in geophysical records, *Geophysics,* **68**(3), 1083–1090.

Butler, K.E., Russell, R.D., Kepic, A.W. & Maxwell, M., 1996. Measurement of the seismoelectric response from a shallow boundary, *Geophysics,* **61**(6), 1769–1778.

Butler, K.E., Dupuis, J.C. & Kepic, A.W., 2007. Improvements in signal-to-noise in seismoelectric acquisition, in *Proceedings of Exploration 07*, Toronto, pp. 1137–1141.

Butler, K.E., Kulessa, B. & Pugin, A., 2013. Multiple seismoelectric modes generated by explosive and vibroseis sources in clay-rich sediment, in *Symposium on the Application of Geophysics to Engineering and Environmental Problems (SAGEEP 2013)*, Denver.

Butler, K.E., Kulessa, B. & Pugin, A., 2014. Field evidence for a hybrid interfacial-coseismic seismoelectric effect, in *AGU Fall Mtg.*, San Francisco, CA.

Dean, T. & Dupuis, J.C., 2011. The vibroelectric method - a new tool for near-surface characterisation and improved seismic data quality, in *73rd EAGE Conference Expanded Abstracts*, Vienna.

Dean, T., Dupuis, C., Hermann, R. & Valuri, J., 2012. A brute-strength approach to improving the quality of seismoelectric data, Society of Exploration Geophysicists Technical Program Expanded Abstracts 2012, pp. 1–6.

Dupuis, J.C. & Butler, K.E., 2006. Vertical seismoelectric profiling in a borehole penetrating glaciofluvial sediments, *Geophys. Res. Lett.,* **33**(16), L16301, doi:10.1029/2006GL026385.

Dupuis, J.C., Butler, K.E. & Kepic, A.W., 2007. Seismoelectric imaging of the vadose zone of a sand aquifer, *Geophysics,* **72**(6), A81–A85.

Dupuis, J.C., Butler, K.E., Kepic, A.W. & Harris, B.D., 2009. Anatomy of a seismoelectric conversion: measurements and conceptual modeling in boreholes penetrating a sandy aquifer, *J. geophys. Res.,* **114**(B10), B10306, doi:10.1029/2008JB005939.

El Khoury, P., Revil, A. & Sava, P., 2015. Seismoelectric beamforming imaging: a sensitivity analysis, *Geophys. J. Int.,* **201**(3), 1781–1800.

Frenkel, J., 1944. On the theory of seismic and seismoelectric phenomena in a moist soil, *J. Phys. (Russian),* **8,** 230–241.

Gadd, N.R., 1986. Lithofacies of Leda clay in the Ottawa Basin of the Champlain Sea, Geological Survey of Canada, Paper 85–21, pp. 44.

Garambois, S. & Dietrich, M., 2001. Seismoelectric wave conversions in porous media: field measurements and transfer function analysis, *Geophysics,* **66**(5), 1417–1430.

Garambois, S. & Dietrich, M., 2002. Full waveform numerical simulations of seismoelectromagnetic wave conversions in fluid-saturated stratified porous media, *J. geophys. Res.,* **107**(B7), ESE 5-1–5-18, doi:10.1029/2001JB000316.

Gershenzon, N., Bambakidis, G. & Ternovskiy, I., 2014. Coseismic electromagnetic field due to the electrokinetic effect, *Geophysics,* **79**(5), E217–E229.

Grobbe, N. & Slob, E., 2016. Seismo-electromagnetic thin-bed responses: natural signal enhancements?, *J. geophys. Res.,* **121**(4), 2460–2479.

Guan, W., Hu, H. & Zheng, X., 2013. Theoretical simulation of the multipole seismoelectric logging while drilling, *Geophys. J. Int.,* **195**(2), 1239–1250.

Haartsen, M.W. & Pride, S.R., 1997. Electroseismic waves from point sources in layered media, *J. geophys. Res.,* **102**(B11), 24745–24769.

Haines, S.S. & Pride, S.R., 2006. Seismoelectric numerical modeling on a grid, *Geophysics,* **71**(6), N57–N65.

Haines, S.S., Pride, S.R., Klemperer, S.L. & Biondi, B., 2007. Seismoelectric imaging of shallow targets, *Geophysics,* **72**(2), G9–G20.

Harrison, J.E. & MacDonald, G., 1980. Generalized bedrock geology, Ottawa-Hull, Ontario and Québec, Geological Survey of Canada, "A" Series Map 1508A, doi:10.4095/109223.

Hunt, C.W. & Worthington, M.H., 2000. Borehole electrokinetic responses in fracture dominated hydraulically conductive zones, *Geophys. Res. Lett.,* **27,** 1315–1318.

Hunter, J.A. *et al.*, 2010. Seismic site classification and site period mapping in the Ottawa area using geophysical methods; Geological Survey of Canada, Open File 6273.

Jouniaux, L. & Zyserman, F., 2016. A review on electrokinetically induced seismo-electrics, electro-seismics, and seismo-magnetics for Earth sciences, *Solid Earth,* **7,** 249–284.

Kepic, A.W. & Butler, K.E., 2002. The art of measuring very low amplitude seismoelectric signals, in *64th Annual Meeting, Expanded Abstracts*, European Association of Geoscientists and Engineers.

Kepic, A. & Rosid, M., 2004. Enhancing the seismoelectric method via a virtual shot gather, in *Society of Exploration Geophysicists Technical Program Expanded Abstracts 2004*, pp. 1337–1340.

Klemperer, S.L., 1987. Seismic noise?reduction techniques for use with vertical stacking: An empirical comparison, *Geophysics,* **52,** 322–334.

Kulessa, B., Murray, T. & Rippin, D., 2006. Active seismoelectric exploration of glaciers, *Geophys. Res. Lett.,* **33,** doi:10.1029/2006GL025758..

Liu, Z., Yuan, L., Zhang, X., Liu, Z. & Wu, H., 2008. A laboratory seismoelectric measurement for the permafrost model with a frozen–unfrozen interface, *Geophys. Res. Lett.,* **35,** doi:10.1029/2008GL035724.

Lo, K.Y., Bozozuk, M. & Law, K.T., 1976. Settlement analysis of the Gloucester test fill, *Can. Geotech. J.,* **13,** 339–354.

Martner, S.T. & Sparks, N.R., 1959. The electroseismic effect, *Geophysics,* **24,** 297–308.

McRostie, G.C. & Crawford, C.B., 2001. Canadian Geotechnical Research Site No. 1 at Gloucester, *Can. Geotech. J.,* **38,** 1134–1141.

Mikhailov, O.V., Haartsen, M.W. & Toksöz, M.N., 1997. Electroseismic investigation of the shallow subsurface: field measurements and numerical modeling, *Geophysics,* **62,** 97–105.

Mikhailov, O.V., Queen, J. & Toksöz, M.N., 2000. Using borehole electroseismic measurements to detect and characterize fractured (permeable) zones, *Geophysics,* **65**(4), 1098–1112.

Neev, J. & Yeatts, F.R., 1989. Electrokinetic effects in fluid-saturated poroelastic media, *Phys. Rev. B,* **40,** 9135–9141.

Oldenburg, D.W. & Li, Y., 1994. Inversion of induced polarization data, *Geophysics,* **9,** 1327–1341.

Oldenburg, D.W. & Li, Y., 1999. Estimating depth of investigation in DC resistivity and IP surveys, *Geophysics,* **64,** 403–416.

Pride, S.R., 1994. Governing equations for the coupled electromagnetics and acoustics of porous media, *Phys. Rev. B,* **50,** 15678–15696.

Pride, S.R. & Haartsen, M.W., 1996. Electroseismic wave properties, *J. acoust. Soc. Am.,* **100,** 1301–1315.

Pride, S.R. & Garambois, S., 2002. The role of Biot slow waves in electroseismic wave phenomena, *J. acoust. Soc. Am.,* **111,** 697–706.

Pugin, A.J.-M. & Yilmaz, O., 2017. There is no pure *P*- or *S*-wave land seismic source, in *Society of Exploration Geophysicists Technical Program Expanded Abstracts 2017*, pp. 5162–5166.

Pugin, A.J.-M., Pullan, S.E. & Hunter, J.A., 2009. Multicomponent high-resolution seismic reflection profiling, *Leading Edge,* **28,** 1248–1261.

Pugin, A.J.-M., Brewer, K., Cartwright, T., Pullan, S.E., Didier, P., Crow, H. & Hunter, J.A., 2013. Near surface *S*-wave seismic reflection profiling–new approaches and insights, *First Break,* **31,** 49–60.

Ren, H., Huang, Q. & Chen, X., 2016. Existence of evanescent electromagnetic waves resulting from seismoelectric conversion at a solid–porous interface, *Geophys. J. Int.,* **204,** 147–166.

Revil, A. & Jardani, A., 2010. Seismoelectric response of heavy oil reservoirs: theory and numerical modelling, *Geophys. J. Int.,* **180,** 781–797.

Revil, A., Jardani, A., Sava, P. & Haas, A., 2015. *The Seismoelectric Method: Theory and Application,* John Wiley & Sons, Ltd.

Sava, P.C., Revil, A. & Karoulis, M., 2014. High definition cross-well electrical resistivity imaging using seismoelectric focusing and image-guided inversion, *Geophys. J. Int.,* **198,** 880–894.

Schakel, M.D., Smeulders, D.M.J., Slob, E.C. & Heller, H.K.J., 2011. Seismoelectric interface response: experimental results and forward model, *Geophysics,* **76,** N29–N36.

Siegert, M.J., Kulessa, B., Bougamont, M., Christoffersen, P., Key, K., Andersen, K.R., Booth, A.D. & Smith, A.M., 2017. Antarctic subglacial groundwater: a concept paper on its measurement and potential influence on ice flow, in *Exploration of Subsurface Antarctica: Uncovering Past Changes and Modern Processes,* Vol. 461, eds, Siegert, M.J., Jamieson, S.S.R. & White, D.A., Geological Society, London, Special Publications.

Singer, J., Saunders, J., Holloway, L., Stoll, J.B., Pain, C., Stuart-Bruges, W. & Mason, G., 2006. Electrokinetic logging has the potential to measure permeability, *Petrophysics,* **47**(5) 427–441.

Strahser, M.H.P., Rabbel, W. & Schildknecht, F., 2007. Polarisation and slowness of seismoelectric signals, a case study, *Near Surf. Geophys.,* **5,** 97–114.

Strahser, M.H.P., Journiaux, L., Sailhac, P., Matthey, P.-D. & Zillmer, M., 2011. Dependence of seismoelectric amplitudes on water content, *Geophys. J. Int.,* **187,** 1378–1392.

Thompson, A.H. & Gist, G.A., 1993. Geophysical applications of electrokinetic conversion, *Leading Edge,* **12,** 1169–1173.

Thompson, A.H. *et al.*, 2007. Field tests of electroseismic hydrocarbon detection, *Geophysics,* **72,** N1–N9.

Thompson, S., Kulessa, B. & Luckman, A., 2012. Integrated electrical resistivity tomography (ERT) and self-potential (SP) techniques for assessing hydrological processes within glacial lake moraine dams, *J. Glaciol.,* **58,** 849–858.

Warden, S., Garambois, S., Jouniaux, L., Brito, D., Sailhac, P. & Bordes, C., 2013. Seismoelectric wave propagation numerical modelling in partially saturated materials, *Geophys. J. Int.,* **194,** 1498–1513.

West, M.T.N., 2012. Seismoelectric experiments in a natural laboratory: comparisons of theoretical and measured transfer functions for co-seismic arrivals, *MSc Thesis*, University of New Brunswick, Fredericton, Canada.

Zhu, Z. & Toksöz, M.N., 2003. Crosshole seismoelectric measurements in borehole models with fractures, *Geophysics,* **68,** 1519–1524.

Zhu, Z. & Toksöz, M.N., 2013. Experimental measurements of the streaming potential and seismoelectric conversion in Berea sandstone, *Geophys. Prospect.,* **61,** 688–700.

Zyserman, F.I., Jouniaux, L., Warden, S. & Garambois, S., 2015. Borehole seismoelectric logging using a shear-wave source: Possible application to CO2 disposal?, *Int. J. Greenhouse Gas Control,* **33,** 89–102.